Lithospheric Control of Melt Generation Beneath the Rungwe Volcanic Province, East Africa

Emmanuel A. Njinju[1]*, D. Sarah Stamps[1], Kodi Neumiller[2], and James Gallager[2]

[1]Department of Geosciences, Virginia Tech, Blacksburg, VA, USA

[2]OPeNDAP, Narragansett, RI, USA

*Corresponding author: Emmanuel A. Njinju (njinju85@vt.edu)

Keywords:

- Lithospheric modulated convection; Melt generation; Rungwe Volcanic Province; Malawi Rift; East African Rift

Key Points:

- Decompression melting from lithospheric modulated convection provides a source of deep melt for the Rungwe Volcanic Province, East Africa
- Lithospheric modulated convection likely entrains materials from deeper plume sources beneath the Rungwe Volcanic Province
- A plume that penetrates the transition zone beneath the Rungwe Volcanic Province is not required to explain geochemical and geophysical observations

Abstract

The Rungwe Volcanic Province (RVP) is a volcanic center in an anomalous region of magma-assisted rifting positioned within the magma-poor Western Branch of the East African Rift (EAR). The source of asthenospheric melt for the RVP is enigmatic, particularly since the volcanism is highly localized, unlike the Eastern Branch of the EAR. Some studies suggest the source of asthenospheric melt beneath the RVP arises from thermal perturbations in the upper mantle associated with an offshoot of the African Superplume flowing from the SW, while others propose a similar mechanism, but from the Kenyan plume diverted around the Tanzania Craton from the NE. Another possibility is decompression melting from upwelling asthenosphere due to lithospheric modulated convection (LMC) where the lithosphere is thin. We test the hypothesis that asthenospheric melt feeding the RVP can be generated from LMC. We develop a 3D thermomechanical model of LMC beneath the RVP and the entire Malawi Rift that incorporates melt generation. We assume a rigid lithosphere with laterally varying thickness and use non-Newtonian, temperature-, pressure- and porosity-dependent creep laws of anhydrous peridotite for the sublithospheric convecting mantle. We find decompression melt associated with LMC upwelling (~3 cm/yr) occurs at a maximum depth of ~150 km localized beneath the RVP. We also suggest asthenospheric upwelling due to LMC entrains plume materials that do not penetrate the transition zone into the melt. Decompression melting associated with upwelling due to LMC may also provide melt sources for other continental regions of thinned lithosphere.

1. Introduction

Melt intrusions into the lithospheric mantle and crust during extensional tectonics play a key role in weakening the lithosphere during magma-assisting rifting. Magma-assisted continental rifting involves magmatic intrusions that are sourced from melt generated in the upper asthenosphere beneath the rift axis, which develops when mantle potential temperatures are higher than average (i.e. McKenzie & Bickle, 1988). The source of melt generation in the upper asthenosphere beneath rifts has been proposed to originate from thermal perturbations due to plumes (e.g. Burke & Dewey, 1973; Furman et al., 2006; Saunders et al., 1992) or asthenospheric upwelling in response to thinned, extended lithosphere (e.g. Nielsen & Hopper, 2002; van Wijk et al., 2001;White & McKenzie, 1989).

The magma-poor Malawi Rift, which is the southernmost rift segment of the Western Branch of the East African Rift (EAR; Figure 1), provides a natural laboratory to investigate the source of asthenospheric melt. In particular, the source of sublithospheric melt for the Rungwe Volcanic Province (RVP), located in the northern region of the Malawi Rift, is contentious. Based on P and S wave seismic tomography, Grijalva et al. (2018) hypothesize deep melt beneath the RVP arises from flow of warm, mantle superplume rising from the southwest that upwells beneath and diverts around the thick lithosphere of the Bangweulu cratonic block. In contrast, thermomechanical modeling by Koptev et al. (2018) suggests that the melt beneath the RVP is sourced from the Kenyan plume that is channeled into three mantle flows by the thick lithospheric keel of the Tanzanian craton and the Bangweulu cratonic block. Alternatively, Yu et al. (2020) suggest passive mantle upwelling distinct from plume sources explains upper mantle 3D seismic velocity and radial anisotropy structures. We hypothesize that the melt beneath the

RVP is, at least, partly generated from decompression melting associated with the passive upwelling model.

Here, we produce a 3D regional thermomechanical geodynamic model of passive upwelling driven by lithospheric modulated convection (LMC) beneath the RVP and the Malawi Rift using ASPECT (Advanced Solver for Problems in Earth's ConvecTion; Bangerth et al., 2018a; Bangerth et al., 2018b; Heister et al., 2017; Rose et al., 2017) to test the latter hypothesis. LMC is asthenospheric convection generated from temperature variations due to lateral variations in lithospheric thickness. An isotherm is assumed for the base of the lithosphere with an approximate adiabatic increase in temperature below the lithosphere. The model also takes into account rheological flow laws that allow for the generation of sublithospheric melts in a continental setting.

This study is part of the EarthCube project BALTO (Brokered Alignment of Long-Tail Observations), which is aimed at developing new, state-of-art cyberinfrastructure that enables brokered access to diverse geoscience datasets. One of the BALTO developments is a new plug-in for the community extensible NSF open-source finite element code ASPECT that permits the user to access data on the internet using web services from any remote server that uses DAP (Data Access Protocol; Gallagher et al., 2004). This study is a use-case of this BALTO cyberinfrastructure, which accesses lithospheric thickness (Fishwick et al., 2010 updated) to constrain LMC and calculate melt generation beneath the RVP and the Malawi Rift.

LMC has a pattern upwelling beneath the RVP at rates of up to 3 cm/yr where lithosphere is relatively thin and produces southern asthenospheric flow along the Malawi Rift. We suggest the upwelling may entrain plume materials that do not penetrate the transition zone, which explains high $^{3}He/^{4}He$ detected in RVP lavas (Hilton et al., 2011). A significant percentage of

asthenospheric melt from LMC occurs at depths of ~130 – 155 km localized beneath the RVP, consistent with the location and maximum depth (<200 km) of slow P-wave velocity anomalies beneath the RVP (Yu et al., 2020). These results suggest a plume head that penetrates the transition zone is not required to explain available geochemical and geophysical observations of the Malawi Rift. The source of asthenospheric melt from LMC provides a source for shallower lithospheric intrusions of magma that weaken the lithosphere (i.e. Buck, 2006), thereby enabling magma-assisted rifting in the northern Malawi Rift. Our results indicate LMC is also a likely source of melt for volcanoes in continental regions underlain by shallow lithosphere.

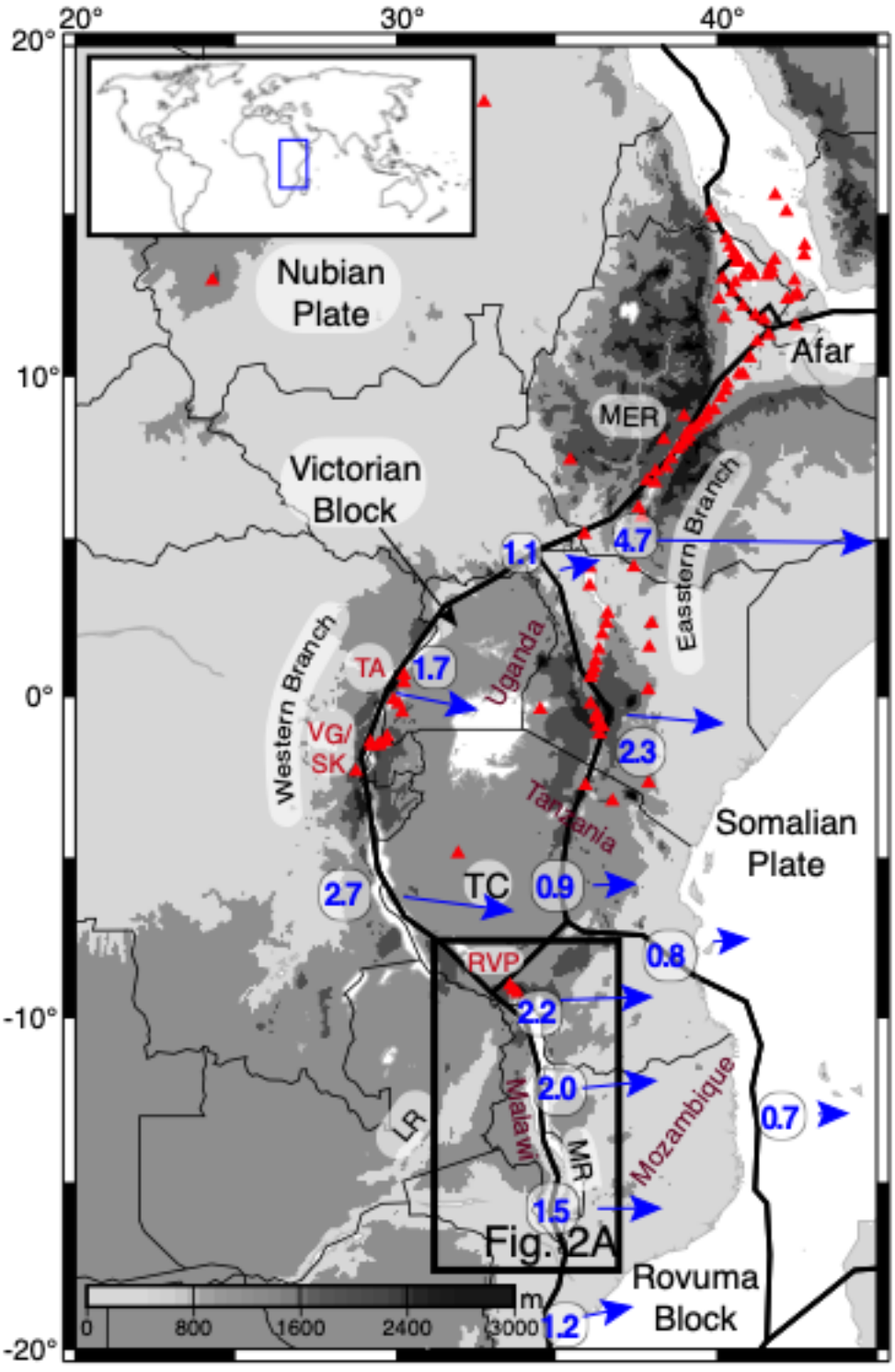

Figure 1. Digital Elevation Model (DEM) extracted from the Global 30 arc second Elevation Data (GTOPO30; DAAC, 2004) showing the Eastern and Western Branches of the East African Rift (EAR). The Eastern Branch of the EAR shows more volcanic centers (red triangles) than the Western Branch. MER = Main Ethiopian Rift. TC = Tanzanian Craton. MR = Malawi Rift. LR =

Luangwa Rift. Red labels indicate volcanic centers in the Western Branch. TA = Toro Ankole. VG/SK = Virunga and South Kivu. RVP = Rungwe Volcanic Province. The black rectangle labeled Fig. 2A indicates the study area shown in Figure 2A. Blue vectors are predicted velocities representing surface motion (mm/yr) relative to the Nubian Plate from Saria et al. (2014). Black thin lines delineate international borders with the names of the main countries transect by the Western Branch labeled in brown colors. The inset map shows the relative location of part of the EAR (blue rectangle) on Earth.

2. Tectonic Setting

2.1. The Malawi Rift

The Malawi Rift, which represents the southern prolongation of the Western Branch of the EAR (Figure 1), is a weakly extended rift (stretching factor of ~1.54; Njinju et al., 2019b) that spans ~900 km from southern Tanzania, through Malawi, to northern Mozambique. The Malawi Rift (Figure 2A) is characterized by asymmetric half grabens bounded by curvilinear border faults with records of deep seismicity suggesting that the border faults extend to the base of the crust (Craig et al., 2011; Ebinger et al., 2019). Indeed, geophysical studies reveal a thick crust (~38 – 45 km; Borrego et al., 2018; Njinju et al., 2019b) and a relatively strong and thick lithosphere beneath the central Malawi Rift (~115 – 210 km; Fishwick, 2010 updated; Njinju et al., 2019b). Geodetic studies, suggest that the rift is opening at a surface velocity of 2.2 mm/yr in the north and 1.5 mm/yr in the south due to an eastward movement of the Rovuma Plate away from the Nubian Plate (Figure 1; i.e. Stamps et al., 2008; Saria et al., 2014). The rift is largely magma-poor with volcanism limited to the Pliocene-Pleistocene RVP located in the northern tip of the rift (e.g. Furman, 2007; Fontijn et al., 2012). It is possible that magmatism beneath the RVP contributes to the relatively fast spreading rate of the northern segment of the Malawi Rift.

2.2. The Rungwe Volcanic Province

The RVP is the southernmost volcanic region in the Western Branch of the EAR (Figure 1), which lies at the northern tip of the Malawi Rift at the intersection of the Rukwa Rift and Usangu Rift, and covers approximately 1500 km^2 (Figure 2B; Ebinger et al., 1989, 1997; Fontijn et al., 2012). The RVP comprises three large active volcanoes (Ngozi, Rungwe and Kyejo; Figure 2B) in addition to more than 100 cones and domes (Fontijn et al., 2010; Harkin, 1960). The RVP lies at the nexus of three major border fault systems including the Livingstone fault of the Malawi Rift, Lupa fault of the Rukwa Rift, and the Usangu border faults, all of which have been active in Miocene-Recent times (Figures 2B; Fotijn et al., 2012).

The relationship between the tectonic structures in the region and magmatism remains controversial (Mesko et al., 2014; Roberts et al., 2012). Ebinger et al. (1989, 1993) suggest that volcanism in the RVP was synchronous with initial faulting and that local deflections in the state-of-stress might result from plate bending under the load of the volcanoes. Radiometric studies of samples from the RVP using $^{40}Ar/^{39}Ar$ dating techniques suggest that magmatism in the RVP started by 19 Ma (Mesko et al., 2014; 2020) and possibly as early as 25 Ma (Roberts et al., 2012). Although the onset of rifting in the Malawi and Rukwa Rifts is poorly known, Ebinger et al. (1993) used $^{40}Ar/^{39}Ar$ radiometric dating of samples from the RVP to suggest that faulting along the Livingstone border fault in the northern Malawi Rift started ~8.6 Ma. Moreover, U-Pb zircon ages of sediments from Lake Rukwa suggest reactivation and renewed subsidence in the Rukwa Rift at 8.7 Ma (Hilbert-Wolf et al, 2017). The ages of the RVP suggest that volcanism may predate the estimated onset of faulting along the Livingstone border fault and reactivation of the Rukwa Rift. Indeed, geophysical studies provide evidence that is consistent with thermal weakening of the lithosphere (with associated magmatism) preceding rift-related fault development (Grijalva et al., 2018; Koptev et al., 2018; Yu et al., 2020).

165 The source of the magma beneath the RVP still remains enigmatic. Studies by Grijalva et
166 al. (2018) and Koptev et al. (2018) suggest the presence of a mantle plume beneath the RVP that
167 generates melt. This hypothesis is supported by geochemical evidence from RVP lavas showing
168 elevated mantle potential temperatures (Rooney et al., 2011) and elevated $^{3}He/^{4}He$ isotopic ratios
169 (Hilton et al., 2011). However, Yu et al. (2020) suggest that the melt beneath the RVP arises
170 from decompression melting in response to passive upwelling associated with lithospheric
171 stretching based on relatively shallow low seismic velocity anomalies that are disconnected from
172 seismic anomalies below the transition zone. Our study tests the latter hypothesis.

173

174

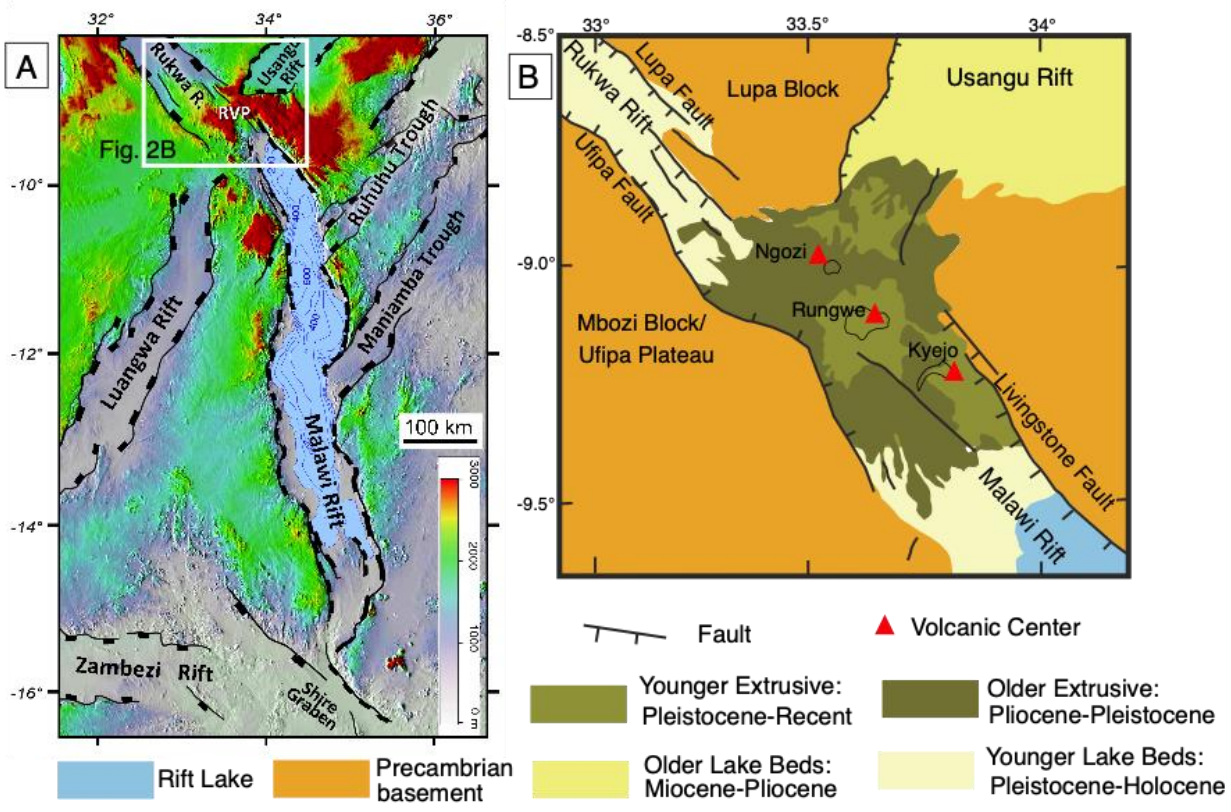

175

Figure 2. (**A**) Shuttle Radar Topography Mission (SRTM) Digital Elevation Model (DEM; Farr et al., 2007) of the Malawi Rift showing the border faults and the surrounding Paleozoic-Mesozoic Karoo rift basins corresponding to the study area (black rectangle) in Figure 1. Blue contour lines show water depth within Lake Malawi. The white box labeled Fig. 2B in Figure 2A shows the location of Figures 2B. RVP = Rungwe Volcanic Province. (**B**) The geological map of the RVP and the surrounding Precambrian basement. Modified after Fotijn et al. (2012). The legend is referencing Figure 2B.

3. Methods

We simulate time-dependent LMC that incorporates melt generation in the asthenosphere and transition zone in a 3D domain using the finite element code ASPECT (Bangerth et al., 2018a; Bangerth et al., 2018b; Heister et al., 2017; Rose et al., 2017) to test the potential role of LMC in asthenospheric melt generation beneath the RVP and the Malawi Rift. Recent studies demonstrate the capabilities of modeling melt generation and magma dynamics in ASPECT (Dannberg et al., 2019; Dannberg & Heister, 2016), however this is the first study that uses present-day lithospheric structure as input to model melt generation associated with LMC.

3.1. 3D Lithospheric Modulated Convection Modeling

3.1.1. Governing Equations

We generate LMC beneath the Malawi Rift by solving for the velocity term **u** of the Stokes flow equation, which is the conservation equation for momentum (Eq. 1) and mass (Eq. 2) for an incompressible fluid:

$$-\nabla \cdot [2\eta\, \varepsilon(\mathbf{u})] + \nabla p = \rho \mathbf{g} \qquad \text{in } \Omega, \tag{1}$$

$$\nabla \cdot \mathbf{u} = 0 \qquad \text{in } \Omega \tag{2}$$

where $\varepsilon(\mathbf{u})$ is the strain rate which is the symmetric gradient of the velocity. p, η, ρ, $\mathbf{g}$ are, respectively, the dynamic pressure, temperature, viscosity, density, and gravitational acceleration. We assume an incompressibility condition for the mass conservation equation (Eq.

2) so that changes in density (e.g., due to pressure and temperature) are negligible. In order to model melt generation, we also simulate changes in temperature caused by heat transfer in the model by solving the energy conservation equation (Eq. 3). We apply the extended Boussinesq approximation that includes shear heating, adiabatic heating, and latent heat of melting in the heating model (Christensen & Yuen, 1985):

$$\rho C_p \left(\frac{\partial T}{\partial t} + \mathbf{u} \cdot \nabla T \right) - \nabla \cdot k \nabla T = 2\eta [\, \varepsilon(\mathbf{u}) \, : \, \varepsilon(\mathbf{u})] + \alpha T \, (\mathbf{u} \cdot \nabla p) + \rho T \Delta S \left(\frac{\partial F}{\partial t} + \mathbf{u} \cdot \nabla F \right) \quad \text{in } \Omega, \tag{3}$$

We assume phase-independent parameterizations for the specific heat C_p and thermal expansivity α, and thermal equilibrium in the entire model. k is the thermal conductivity. Based on previous studies, we assume an average crustal thermal conductivity of k = 2.5 W.m^{-1}.K^{-1} (Njinju et al., 2019a). For the lithospheric mantle, we assume an average thermal conductivity of 3.5 W.m^{-1}.K^{-1} (Burov, 2011; Koptev et al., 2018) and a thermal conductivity of 4.7 W.m^{-1}.K^{-1} for the sublithospheric mantle (Clauser & Huenges, 1995; Dannberg & Heister, 2016). The latent heat consumed during melting is proportional to changes in the melt fraction F and the entropy change ΔS. The latent heat of melting is incorporated, with an entropy change of ΔS = -300 J.kg^{-1}.K^{-1} (Dannberg & Heister, 2016). The buoyancy force driving mantle convection is proportional to both the density of the fluid and the gravitational acceleration. Although we assume incompressible flow for the mass conservation equation (Eq. 2), the density in the buoyancy term varies with both temperature and pressure:

$$\rho = \rho(T, p) = \rho_0 [1 - \alpha(T - T_0)] \exp [\beta(p - p_0)] \tag{4}$$

where β is the compressibility coefficient, ρ_0 is the reference density at reference temperature T_0 and reference pressure p_0. We normalize the pressure to a surface pressure of $p_0 = 10^5$ Pa (Yang et al., 2018). For the Earth's mantle, $\rho_0 = 3300$ kg/m^3, $T_0 = 293$ K, $\alpha = 2 \times 10^{-5}$ K^{-1}, $C_p = 1250$ J.kg^{-1}.K^{-1}, and $\beta = 4.2 \times 10^{-12}$ Pa^{-1}.

3.1.2. Model Setup

Our model domain has dimensions of 550 x 1000 x 660 km along latitude, longitude, and depth, respectively, for a spherical chunk geometry (Figure 3B). However, our regions of interest beneath the RVP and the entire Malawi Rift are distant from the model boundaries so that boundary effects are limited. Based on previous tests of edge-effects on the interior of the model due to different velocity boundary conditions (free slip versus zero velocity; Njinju et al. 2019b); we set the velocities at all the sides of the model to zero which exerts minimal edge-effects on the model interior from the boundaries of the model. We refine the entire model domain to a global mesh refinement of 6 such that each element is ~ 8 x 15 x 10 km with 17.5 million unknowns computed on 120 cores. The model is comprised of a lithosphere and an underlying mantle that extends to 660 km depth, which includes the transition zone.

The lithospheric structure is read from the BALTO site by the BALTO-ASPECT plugin using the web services provided by the BALTO broker. The lithosphere is part of the updated lithospheric structure model of Fishwick (2010) mapped into the 3D domain for the Malawi Rift and surroundings (Figure 3A). The lithosphere is thinnest beneath the RVP at the northern tip of the Malawi Rift (~100 km) and also beneath the southern rift segment (~100-125 km). The lithosphere is thickest beneath the central segment of the Malawi Rift (~175-200 km). The lithospheric structure produces lateral variations in temperature and pressure such that relatively thin lithosphere has hotter geothermal gradients and lower overburden pressure than the thicker

lithosphere, which is relatively colder and exerts a higher lithostatic pressure. The temperature and pressure variations due to variations in the lithospheric thickness lead to lateral density perturbations in the asthenosphere and transition zone that drive LMC (Eq. 4).

The initial temperature structure (Figure 3B) includes an approximation of a conductive geotherm for the lithosphere with a linear temperature gradient from the surface (T_0 = 293 K) to the base of the lithosphere, which is an isothermal boundary defined by the mantle potential temperature T_p (Figure 5). The mantle potential temperature, T_p is the temperature that the mantle would have at the surface if ascended along an adiabat without melting (McKenzie & Bickle, 1988). The T_p in the RVP from eruptions occurring in the past 10 Ma ranges from ~1420-1450 °C (~1693 - 1723 K) based on the geochemical observations of Rooney et al. (2011). We test a range of T_p (1693, 1703, 1713, 1723 K) and find that T_p = 1723 K produces a geotherm hot enough to generate melt (Figure S1; see supporting information for details). Below the lithosphere, the temperature increases approximately adiabatically (0.5 K/km) to the base of the model (Figure 5).

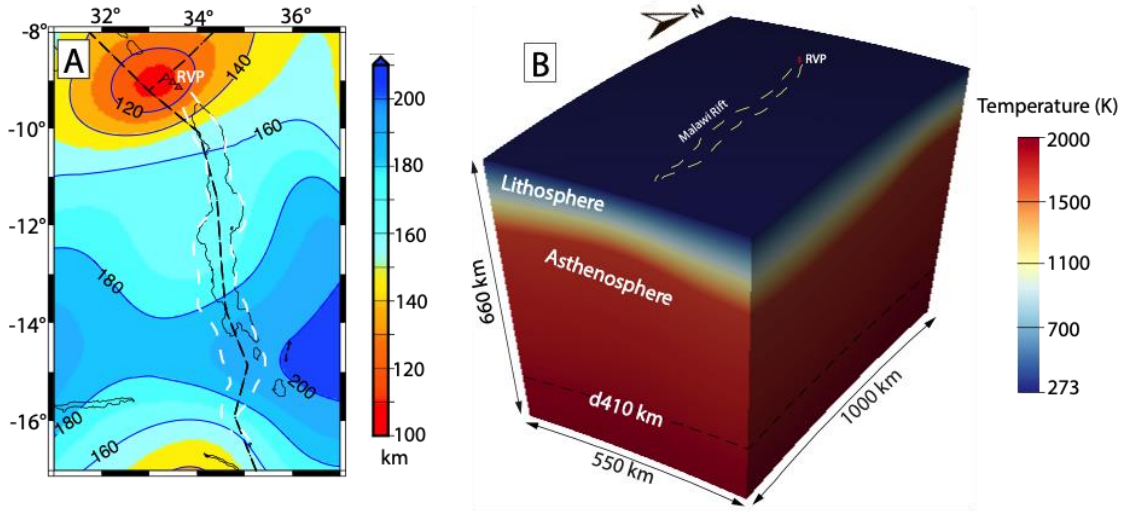

Figure 3. (**A**) Lithospheric thickness map of the Malawi Rift and surroundings, updated from Fishwick (2010) which we use as input in this study. The blue contours show lines of equal lithospheric thickness at 20 km intervals. Black dotted lines represent plate boundaries from Stamps et al. (2008). White dotted lines indicates the outline of the Malawi Rift traced from the Shuttle Radar Topography Mission (SRTM) Digital Elevation Model (DEM) (Figure 2A; Farr et al., 2007). (**B**) Numerical model setup showing the model dimensions and the initial temperature condition as the background in 3D. Yellow dotted lines shows the outline of the Malawi Rift. RVP = Rungwe Volcanic Province.

3.1.3. Rheology

Mantle convection is highly dependent on the viscosity. Since we are interested in LMC in the asthenosphere and transition zone, we impose a strong, uniform viscosity of 10^{23} Pa.s for the lithosphere (Figures 4A and 4B). For the asthenosphere, we use non-Newtonian, temperature-, pressure- and porosity-dependent creep laws of anhydrous peridotite. Unlike the viscosity model of Keller et al. (2013), which is given by the application of an exponential melt-weakening factor to a constant background mantle viscosity of 10^{22} Pa.s, we assume the background viscosity of the sublithospheric mantle is governed by composite rheology for dry olivine material parameters (Jadamec & Billen, 2010; Rajaonarison et al., 2020). The composite rheology (η_{comp}) is the harmonic average of the viscosity from dislocation-creep (η_{disl}) and diffusion-creep (η_{diff}) flow laws of dry olivine and is given by:

$$\eta_{\text{diff, disl}} = \frac{1}{2} A^{-\frac{1}{n}} d^{\frac{m}{n}} \dot{\epsilon}^{\frac{1-n}{n}} \exp\left(\frac{E_a + pV_a}{nRT}\right) \quad (5)$$

$$\eta_{\text{comp}} = \frac{\eta_{\text{diff}} \cdot \eta_{\text{disl}}}{\eta_{\text{diff}} + \eta_{\text{disl}}} \quad (6)$$

where A is the prefactor, n is the stress exponent, $\dot{\epsilon}$ is the square root of the second invariant of the deviatoric strain rate tensor, d is the grain size, m is the grain size exponent, E_a is the activation energy, V_a is the activation volume, p is pressure, R is the gas constant, and T is the

282 temperature. The values for the parameters A, n, m, E_a and V_a are obtained from experimental
283 studies of dry olivine (Hirth & Kolhstedt, 2004; Table 1). The viscosity of the sublithospheric
284 mantle ($\eta_{\text{sublith-mantle}}$) with porosity dependence is given by:

285 $$\eta_{\text{sublith-mantle}} = \eta_{\text{comp}} \cdot \exp[-\alpha_{\Phi}\Phi] \quad (7)$$

286 where the exponential melt-weakening factor is experimental constrained to $25 \leq \alpha_{\Phi} \leq 30$ (Mei et
287 al., 2002). We use the average value of $\alpha_{\Phi} = 27.5$. The porosity Φ is the ratio of the volume of
288 pore spaces between the olivine grains of peridotite to the bulk volume of the peridotite
289 constituent of the asthenosphere. The material properties for each layer (lithosphere and
290 sublithospheric mantle) are tracked through compositional fields with the asthenosphere and
291 transition zone further divided into two compositional fields called “porosity” and “peridotite”.
292 The porosity in the model is tracked through the compositional field “porosity”. The viscosity at
293 each quadrature point is calculated from the harmonic average of the compositional fields
294 weighted by the volume fraction of each composition at the same location (Figures 4A and 4B;
295 Rajaonarison et al., 2020).

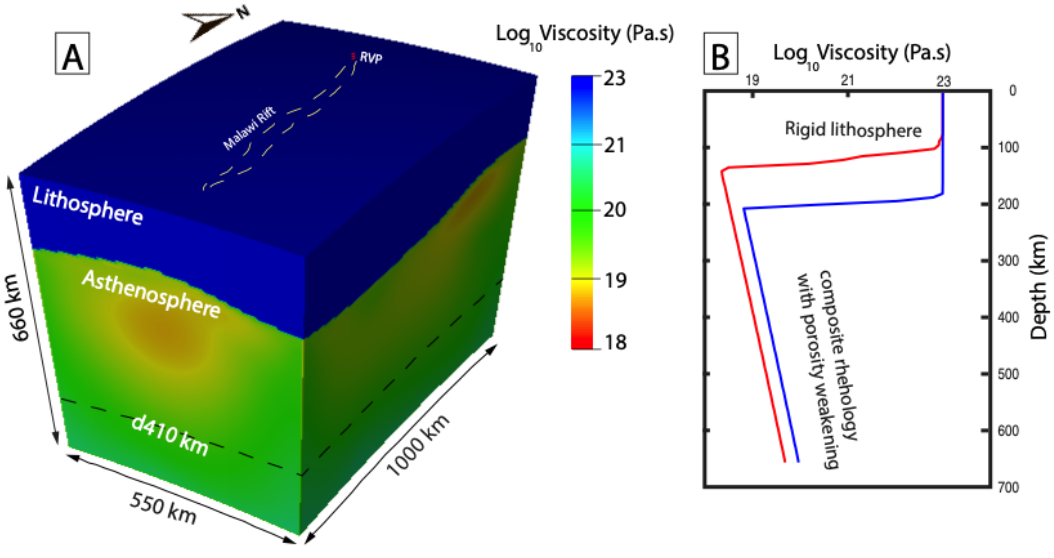

296

297 **Figure 4**. (**A**) Three-dimensional representation of the initial viscosity field. Yellow dotted lines
298 show the outline of the Malawi Rift. RVP = Rungwe Volcanic Province. (**B**) One-dimensional
299 initial viscosity depth profiles for a lithospheric thickness of 100 km (red) and 200 km (blue).
300

301 Setting the velocities at the bottom boundary to zero approximates the effect of the high viscosity
302 jump across the transition zone on slowing mantle flow velocities (410 – 660 km; Ballmer et al.,
303 2007; Rajaonarison et al., 2020). The temperature boundary conditions at all boundaries are fixed
304 so that the net heat flux at the boundaries is zero following Rajaonarison et al. (2020).

Table 1. Rheological Parameters for Dry Olivine Used in the Viscosity Flow Law of the Sublithospheric Mantle

Parameter	Symbol	Dislocation creep	Diffusion creep	Unit
Activation energy	E_a	530×10^3	375×10^3	J/mol
Activation volume	V_a	18×10^{-6}	6×10^{-6}	m^3/mol
Grain size	d	-	10×10^{-3}	m
Grain size exponent	m	-	3	-
Stress exponent	n	3.5	1.0	-
Prefactor	A	7.4×10^{-15}	4.5×10^{-15}	$Pa^{-n}m^m s^{-1}$

305

306 3.2. Partial Melting

307 For efficient modeling of melt generation in the asthenosphere, we model melting of
308 anhydrous peridotite according to Katz et al. (2003), which is valid for shallow upper mantle
309 melting beneath continental lithosphere. Partial melting in the asthenosphere is highly dependent

on the mantle potential temperature, T_p (Figure 5; McKenzie & Bickle, 1988), and will occur if the T_p is such that adiabatically ascending mantle intersects the solidus (Figure 5). The derived melt fraction $F(p, T)$ depends on the lithostatic pressure p (Pa) and temperature T (K) and is given by:

$$F(p, T) = [(T - T_{solidus})/(T_{liquidus} - T_{solidus})]^{1.5}, \text{ at } T_{solidus} \leq T \leq T_{liquidus} \quad (8a)$$

where the mantle solidus temperature $T_{solidus}$ and liquidus temperature $T_{liquidus}$ are respectively given by:

$$T_{solidus} = A_1 + A_2\, p + A_3\, p^2, \quad (8b)$$

$$T_{liquidus} = B_1 + B_2\, p + B_3\, p^2, \quad (8c)$$

where A_1 = 1085.7 K, A_2 = 1.329 x 10^{-7} K/Pa, A_3 = -5.1 x 10^{-18} K/Pa^2, B_1 = 1475.0 K, B_2 = 8.0 x 10^{-8} K/Pa, and B_3 = -3.2 x 10^{-18} K/Pa^2.

Partial melting in the asthenosphere is also highly dependent on the lithospheric thickness. This is because a thick lithosphere serves as a mechanical barrier to adiabatic ascent of hot mantle materials. The thickness of the melt zone and the maximum extent of partial melting are limited by the lithospheric thickness (e.g., McKenzie & O'Nions, 1995). We test the sensitivity of melt generation to lithospheric thickness variations in our model by conducting simulations with varied lithospheric thickness (+10 km and -10 km) based on the model of Fishwick (2010, updated). We find that when we increase the lithospheric thickness by 10 km (increase of mechanical barrier to adiabatic ascent of hot mantle materials) no melt is generated due to LMC (Figure S2). However, when we reduce the lithospheric thickness by 10 km (reduction of mechanical barrier), an unrealistically high melt fraction (~12% melt; Figure S2) is

generated from LMC beneath the RVP (see supplementary material for details). This test also serves as a validation of the lithospheric thickness model by Fishwick (2010), which when used as an input in our model; we obtain a more realistic melt fraction (~1.5% melt) from LMC (see section 4.2). We simulated convection for 20 Ma to ensure that steady state is achieved. The melt that reaches the base of the lithosphere may refreeze, accumulate in a deep or shallow magma reservoirs, inject into the lithosphere as dikes, or erupt to create new crust, however the fate of the melt in the lithosphere is beyond the scope of this study.

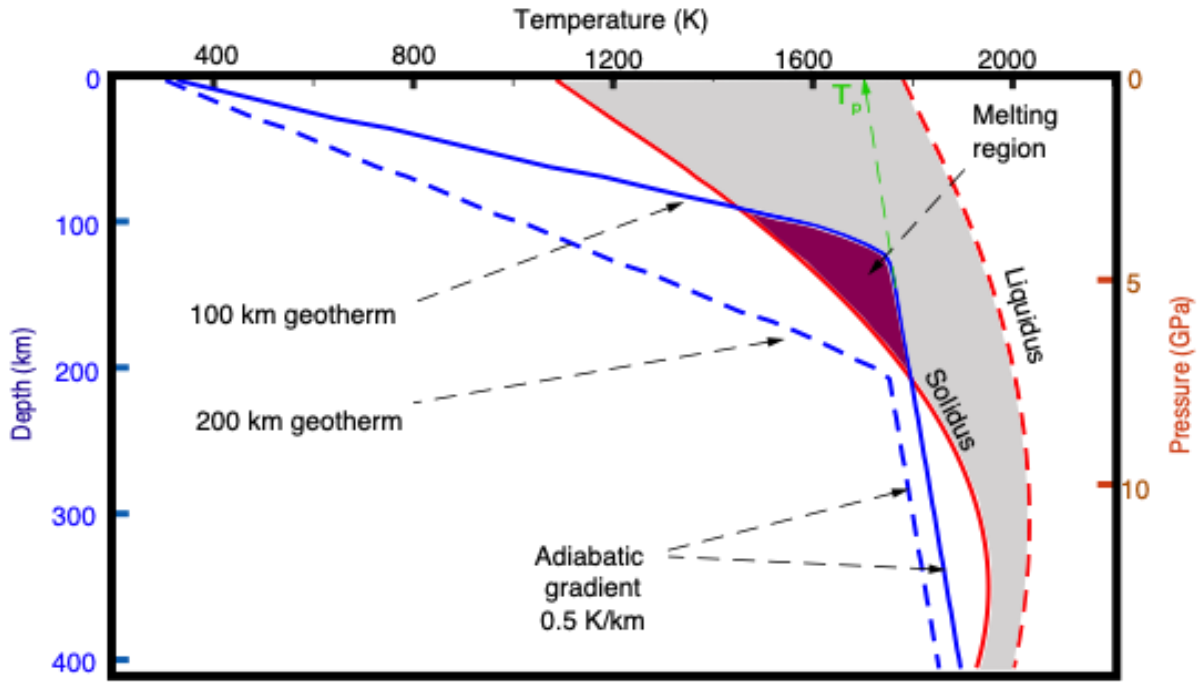

Figure 5. A combined plot of temperature-depth profiles (blue solid lines for a 100 km thick lithosphere and blue-dashed lines for a 200 km thick lithosphere) and a pressure-temperature phase diagram depicting shallow melting of anhydrous peridotite parameterized from Katz et al. (2003). The red solid line represents the solidus (0% melt) and the red-dashed line represents the liquidus (100% melt). The solidus and liquidus are plotted from equations (8b) and (8c) respectively. T_p represents the mantle potential temperature.

4. Results

4.1 Lithospheric Modulated Convection

In our simulation, LMC develops spontaneously from our initial thermal conditions and forms where there is a transition in lithospheric thickness from relatively thick to thin (see Figure 3A). Figures 6A and 6B show flow patterns at 17 Ma (time during which the flow is steady-state; see section 4.2) resulting from our numerical modeling of LMC at 150 km and 250 km depth slices, respectively. Asthenospheric upwelling occurs beneath thin lithosphere, while downwelling occurs beneath relatively thick lithosphere. Our results indicate asthenospheric upwelling beneath the RVP driven by LMC. At 150 km depth (Figure 6A), asthenospheric upwelling (~1 cm/yr) with a diverging (~2 cm/yr) horizontal flow occurs only beneath the RVP where the lithosphere is thin (~100-120 km). At 250 km depth (Figure 6B), the asthenospheric upwelling beneath the RVP is faster (~3 cm/yr). Another zone of weaker upwelling (~0.5 cm/yr) occurs beneath the southern end of the Malawi Rift where the lithosphere is ~160 km thick compared to the thicker lithosphere (~180 km) in the central part of the rift. Our model suggests a southward flow of the upwelling mantle beneath the RVP towards the thick lithosphere in the central part of the Malawi Rift where the asthenospheric flow is characterized by downwelling (Figure 6B). The lithosphere, which is made rigid in the model, is not deforming.

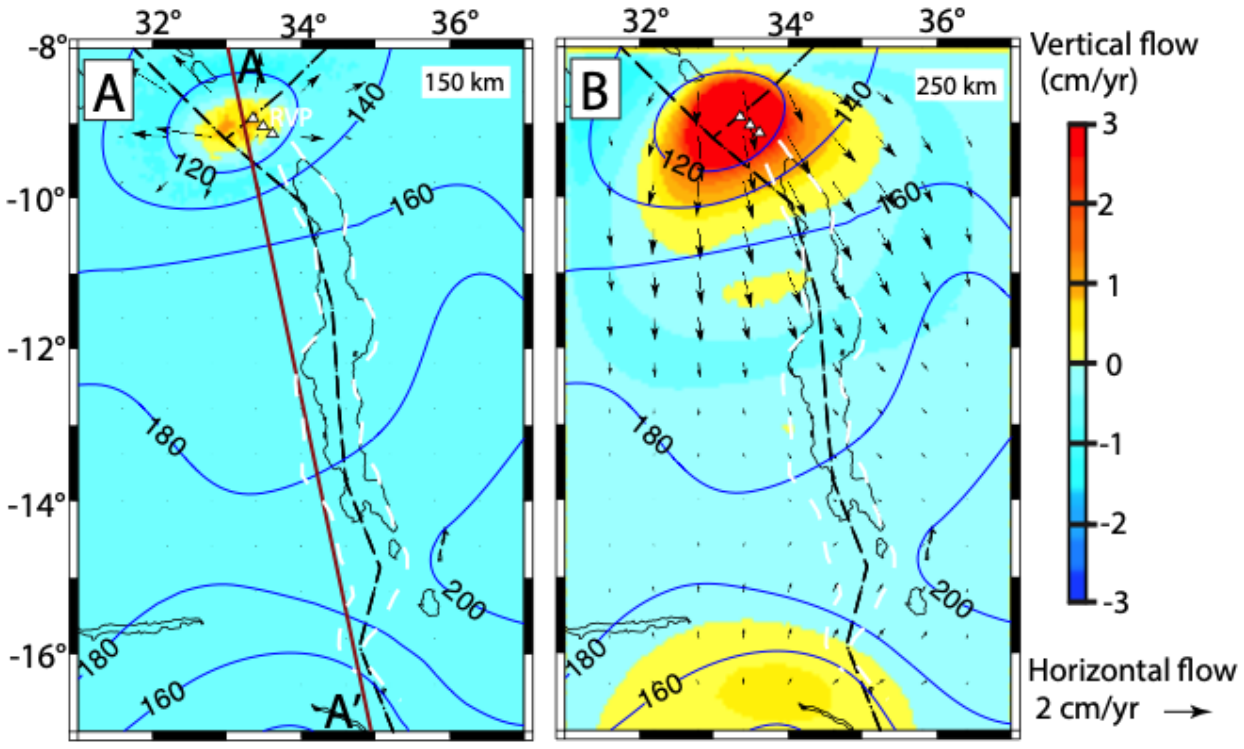

Figure 6. Depth slices showing lithospheric modulated convection beneath the RVP and the Malawi Rift at (**A**) 150 km and (**B**) 250 km depth at 17 Ma. The vertical flow (background color) is overlain by the horizontal flow field (black arrows). White dotted lines indicates the outline of the Malawi Rift traced from the Shuttle Radar Topography Mission (SRTM) Digital Elevation Model (DEM; Farr et al., 2007; Figure 2A). White triangles represent the RVP. Black dotted lines delineate plate boundaries from Stamps et al. (2008). Blue contours show lines of equal lithospheric thickness at 20 km intervals from Fishwick (2010, updated). Brown profile AA' in Figure 6A is the profile location for Figure 8.

4.2 Melt Generation

The time evolution of our melting model (Figure 7) reveals two stages of melting. The first stage, which we call 'the transient or unsteady melting state', occurs in the first 2 Ma of the model evolution beneath the RVP. The instantaneous (0 Ma) decompression melt (~8.5% melt) is not due to LMC; rather the melt arises from the initial conditions, which includes relatively thin lithosphere beneath the RVP and a high mantle potential temperature (1723 K; Rooney et al., 2011). Heat transfer due to LMC controls the duration of melting in the model. During this

382 early stage in our convection model, the initial LMC is unstable and advects most of the heat to
383 the overlying lithosphere. Moreover, there is additional heat loss due to the endothermic melting
384 process such that the asthenosphere experiences a net heat loss. Since the asthenosphere
385 progressively cools, melting sustained by intrinsic density variations decreases rapidly and
386 ceases by 2 Ma (Ballmer et al., 2007). As the model evolves, LMC attains steady-state and
387 asthenospheric upwelling convects hotter mantle materials from the lower part of the
388 asthenosphere and transition zone to shallower sublithospheric depths. This convection leads to
389 the second stage of decompression melting that arises from LMC where the melt fraction
390 increases rapidly from 0 to < 1.5% between 12-16 Ma and saturates to 1.5% melt above 17 Ma
391 (Figure 7).

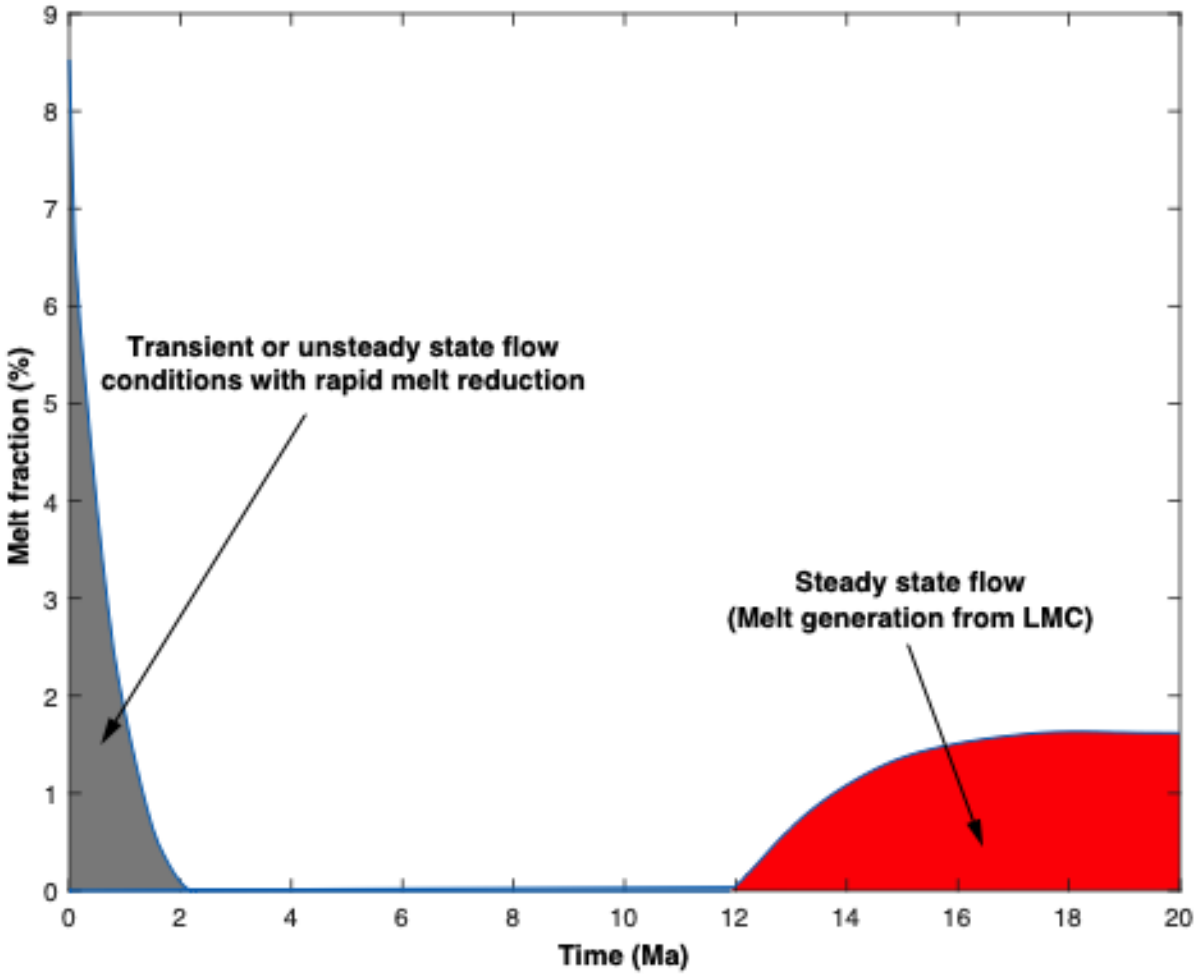

Figure 7. A plot of melt fraction versus time showing the evolution of melt in the model. The gray color (0 – 2 Ma) represents when lithospheric modulated convection (LMC) is unstable and the initial decompression melt (~8.5 %) generated from the initial temperature conditions decreases rapidly and ceases at 2 Ma. The red color (12 – 20 Ma) corresponds to melt generation due to LMC, during which steady-state LMC produces strong upwelling that entrains deep, hot asthenospheric and transition zone materials to shallow, sublithospheric depths.

Figures 8A, 8B and 8C show time-variable LMC and melt generation for the melting parameterization of peridotite (Katz et al., 2003) across the RVP and the long axis of the Malawi Rift (profile AA' defined in Figure 6A). The velocity fields show a similar mantle flow pattern at 10 Ma (Figure 8A), 17 Ma (Figure 8B), and 20 Ma (Figure 8C) with upwelling focused beneath the thin lithosphere of the RVP. The similar flow patterns from 10 – 20 Ma suggest that LMC is

405 stable between 10 and 20 Ma. At 10 Ma (Figure 7A), melt has yet to generate because the LMC
406 has not evolved enough to entrain deep, hot asthenospheric and transition zone materials to
407 shallow sublithospheric depths. At 17 and 20 Ma (Figures 8B and 8C, respectively), upwelling
408 from LMC has had enough time to transport deeper mantle materials to shallower depths, raising
409 the sublithospheric geotherm above the mantle solidus temperature that leads to decompression
410 melting of up to 1.5% melt fractions.

411 Depth slices of the melt model at 17 Ma (Figures 8A, 8B, 8C and 8D) indicate that melt
412 generation due to LMC is restricted to depths of ~130 -155 km beneath the RVP where the
413 lithospheric thickness is <120 km. The maximum melt fraction occurs at the center of the
414 melting region (~145 km) with melt fractions reaching ~1.5% (Figure 8C). Numerical modeling
415 of asthenospheric melt generation beneath the Baikal Rift, which is a relatively magma-poor rift
416 similar to the Malawi Rift, produces similar results of 1 - 2 % melt fractions (Yang et al., 2018).

417

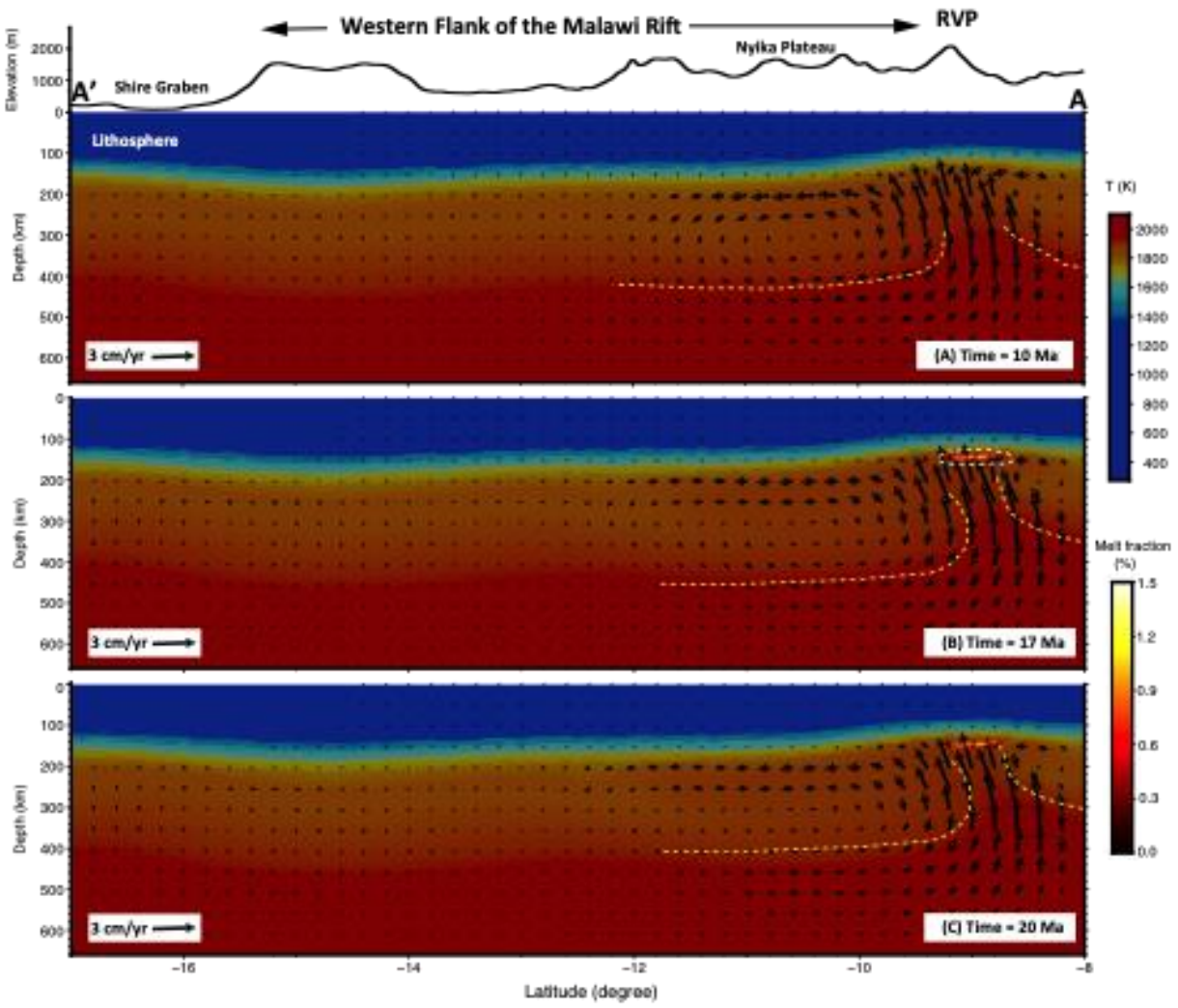

Figure 8. Profile showing time-dependent lithospheric modulated convection (LMC) across the Rungwe Volcanic Province (RVP) and the Malawi Rift (profile AA'; Figure 6A). (**A**) Time = 10 Ma. (**B**) Time = 17 Ma. (**C**) Time = 20 Ma. Note the similarity in the structure of the mantle flow indicating steady-state LMC from 10-20 Ma. We include the yellow dotted lines to help visualize entrainment of deep, hot asthenospheric and transition zone mantle rising to shallower depths beneath the lithosphere.

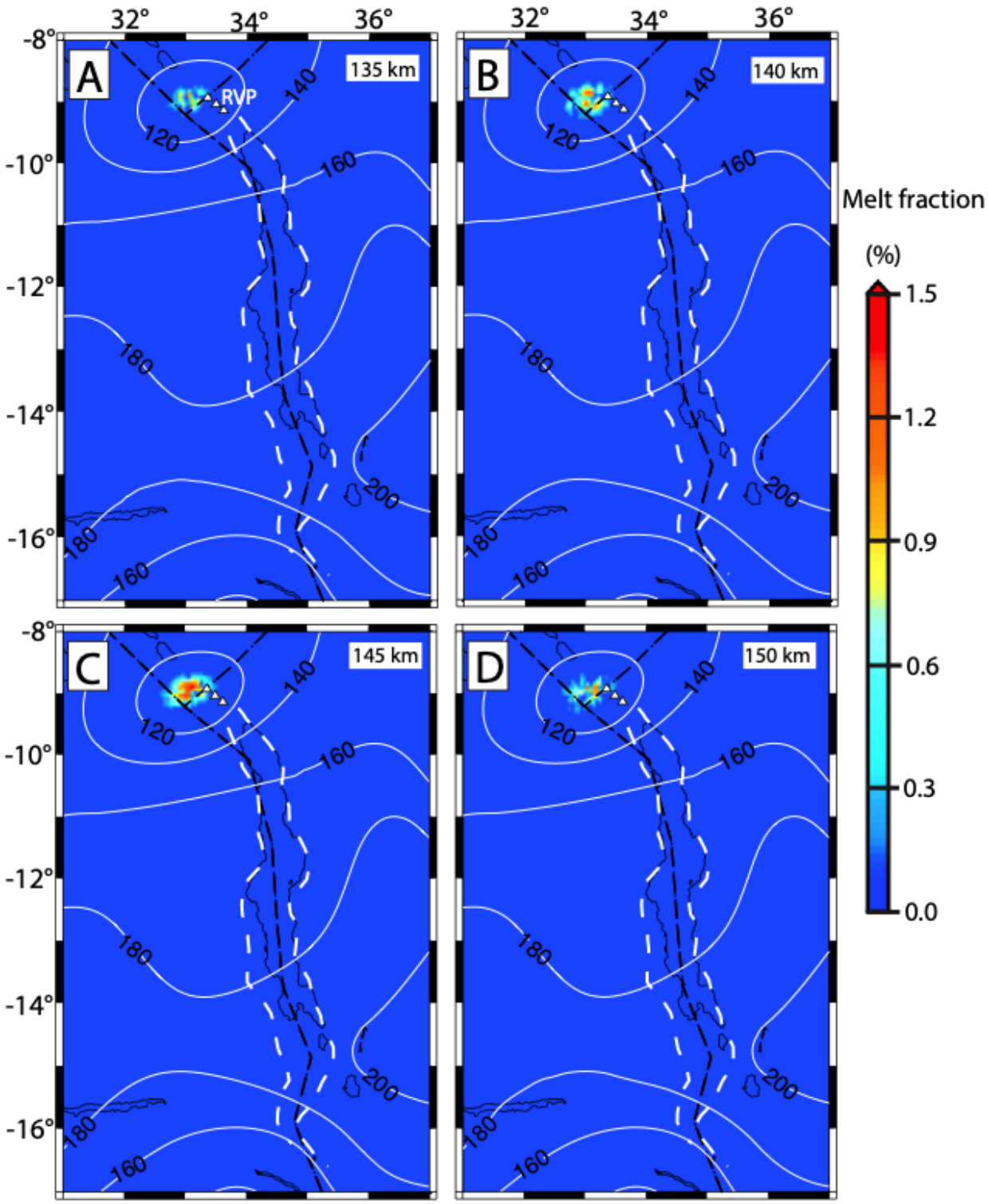

Figure 9. Depth slices showing melt fractions beneath the RVP and the Malawi Rift at (**A**) 135 km, (**B**) 140 km, (**C**) 145 km, and (**D**) 150 km depth at 17 Ma. White dotted lines indicate the outline of the Malawi Rift traced from the Shuttle Radar Topography Mission (SRTM) Digital

Elevation Model (DEM; Farr et al., 2007; Figure 2A). White triangles represent the RVP. Black dotted lines delineate plate boundaries from Stamps et al. (2008). White contours show lines of equal lithospheric thickness at 20 km intervals from Fishwick (2010, updated).

5. Discussion

5.1 Sources of Deep Melt Beneath the Rungwe Volcanic Province

The most prominent features in our model are the isolated region of asthenospheric upwelling and localized decompression melting due to LMC beneath the RVP at depths of ~130 – 155 km. The cross-section of the region of maximum melt generation is roughly elliptical (Figure 8C) with an area of ~4000 km^2. Given that the melting region is roughly conic in shape, the volume of generated melt is ~ 33,000 km^3. The RVP covers an area of ~1500 km^2 (Fotijn et al., 2012) with a maximum elevation of ~2.5 km (Figure 8A). The volume of volcanic rocks covering the RVP is, therefore, generally < 3750 km^3. Thus, the ratio of intrusive versus eruptive melt volume for the RVP is ~ 9:1, which is within the range of intracontinental volcanic fields that is estimated to vary between 4:1 and 10:1 (Crisp, 1984).

The melting region is spatially consistent with a pronounced low velocity anomaly (LVA) beneath the RVP imaged from P-wave anisotropic tomography using data recorded by seismic stations of the Seismic Array for African Rift Initiation experiment (Yu et al., 2020). Yu et al. (2020) found the LVA is mostly constrained to the upper mantle above 200 km depth and has no observable connection with the underlying deeper mantle. This result suggests that the LVA beneath the RVP may be a consequence of partial melts generated from LMC rather than superplume material that rises from the southwest, passes through the transition zone, and impinges the Bangweulu Craton lithosphere where it is then diverted eastward as proposed by Grijalva et al. (2018).

However, a geochemical study of lava and tephra samples from the RVP by Hilton et al. (2011) shows significantly elevated values of helium isotope ratios ($^3He/^4He$) of 15 R_A (R_A = air $^3He/^4He$) which far exceeds typical upper mantle values. The high $^3He/^4He$ ratios associated with the RVP could be sourced from the primordial mantle in the core-mantle boundary brought to the surface by upwelling mantle plumes (Courtillot et al., 2003). Such plume-like $^3He/^4He$ ratios, suggest that a mantle plume contributes to the magmatism beneath the RVP. Upwelling beneath the RVP from LMC likely entrains plume materials that do not penetrate the transition zone and are unresolved by the P-wave tomographic study of Yu et al. (2020). The high mantle potential temperature (1723 K; Rooney et al., 2011) beneath the RVP is also consistent with hot plume materials being entrained into shallow asthenospheric mantle by LMC.

5.2 Implications for Incipient Rifting

Our numerical model of LMC reveals an isolated upwelling beneath the RVP where the lithosphere is thin. This upwelling beneath the RVP results in the production of asthenospheric decompression melt at depths of ~130 - 155 km which is supported by the presence of LVA beneath the RVP that is mostly constrained to the upper mantle above 200 km depth (Yu et al., 2020). The asthenospheric melt may pond beneath the lithosphere and, subsequently, be injected into the mantle lithosphere and crust through preexisting lithospheric structures (Njinju et al., 2019b). Indeed, Accardo et al. (2020) used local measurements of Rayleigh-wave phase velocities to invert for shear wave velocities and clearly observed low velocities (<4.3 km/s) beneath the RVP at crust and upper-mantle depths that are consistent with the presence of injected magma. The injection of magma into the lithosphere is an important factor in the process of continental rift initiation since magma can greatly reduce the strength of thick lithosphere and facilitates rifting (Bastow et al., 2011; Buck, 2006; Kendall et al., 2005; Kendall

& Lithgow-Bertelloni, 2016). Recent seismic tomography models developed for the RVP and the northern Malawi Rift indicate that the lithosphere beneath the Malawi Rift may have been weakened prior to rifting (Accardo et al., 2020; Grijalva et al., 2018; Yu et al., 2020). Southward flow of the upwelling asthenosphere beneath the RVP (Figure 6B) towards the Malawi Rift possibly leads to thermal erosion of the base of the lithosphere, thereby enabling localization of extension in the Malawi Rift (Njinju et al., 2019b).

6. Conclusions

In this study, we develop a 3D thermomechanical model of LMC beneath the RVP and the Malawi Rift that incorporates melt generation. We assume a rigid lithosphere, while for the asthenosphere we use non-Newtonian, temperature-, pressure- and porosity-dependent creep laws of anhydrous peridotite. Our LMC simulation is characterized by an isolated asthenospheric upwelling beneath the RVP, which generates a significant percentage of decompression melt. Our results suggest that the asthenospheric upwelling due to LMC beneath the RVP provides a source of deep melt for these volcanoes. We also suggest LMC entrains deeper plume materials, thus explaining high $^{3}He/^{4}He$ values in the volcanic materials of the RVP and elevated mantle potential temperatures. We, therefore, conclude that asthenospheric upwelling due to LMC beneath the RVP provides an important source of deep melt for the region without necessitating the presence of a plume head penetrating the transition zone. LMC is therefore a likely source of melt for volcanoes in continental regions underlain by shallow lithosphere.

Acknowledgments

This project is supported by the NSF EarthCube Integration grant #1740627. Most of the figures in this paper were generated with Generic Mapping Tools V5.4.2 (Wessel et al., 2013). We also created some of the figures with VISIT v2.9 developed by the Lawrence Livermore National Laboratory. The lithospheric thickness file can be accessed from the Hyrax server through the URL http://balto.opendap.org/opendap/lithosphere_thickness/. The mantle flow models are available at the Open Science Framework repository with doi:…. We thank the Computational Infrastructure for Geodynamics for supporting the development of ASPECT, which is funded by National Science Foundation Awards EAR-0949446 and EAR-1550901.

References

Accardo, N. J., Gaherty, J. B., Shillington, D. J., Hopper, E., Nyblade, A. A., Ebinger, C. J., ... & Russell, J. B. (2020). Thermochemical Modification of the Upper Mantle Beneath the Northern Malawi Rift Constrained From Shear Velocity Imaging. Geochemistry, Geophysics, Geosystems, 21(6), e2019GC008843.

Ballmer, M. D., Van Hunen, J., Ito, G., Tackley, P. J., & Bianco, T. A. (2007). Non-hotspot volcano chains originating from small-scale sublithospheric convection. Geophysical Research Letters, 34(23).

Bangerth, W., Dannberg, J., Gassmoeller, R., & Heister, T. (2018, June 24). Aspect V2.0.1. Zenodo.https://doi.org/10.5281/zenodo.1297145.

Bangerth, W., Dannberg, J., Gassmoeller, R., Heister, T., & Others. (2018). ASPECT: Advanced Solver for Problems in Earth's ConvecTion, User Manual. https://doi.arg/10.6084/m9.figshare.4865333.

Bastow, I. D., & Keir, D. (2011). The protracted development of the continent–ocean transition in Afar. Nature Geoscience, 4(4), 248-250.

Borrego, D., Nyblade, A. A., Accardo, N. J., Gaherty, J. B., Ebinger, C. J., Shillington, D. J., ... & O'Donnell, J. P. (2018). Crustal structure surrounding the northern Malawi rift and beneath the Rungwe Volcanic Province, East Africa. Geophysical Journal International, 215(2), 1410-1426.

Buck, W. R. (2006). The role of magma in the development of the Afro-Arabian Rift System. Geological Society, London, Special Publications, 259(1), 43-54.

544 Burke, K., & Dewey, J. F. (1973). Plume-generated triple junctions: key indicators in applying
545 plate tectonics to old rocks. The Journal of Geology, 81(4), 406-433.

546 Burov, E. B. (2011). Rheology and strength of the lithosphere. Marine and Petroleum Geology,
547 28(8), 1402-1443.

548 Christensen, U. R., & Yuen, D. A. (1985). Layered convection induced by phase transitions.
549 Journal of Geophysical Research: Solid Earth, 90(B12), 10291-10300.

550 Clauser, C., & Huenges, E. (1995). Thermal conductivity of rocks and minerals. Rock physics
551 and phase relations: a handbook of physical constants, 3, 105-126.

552 Courtillot, V., Davaille, A., Besse, J., & Stock, J. (2003). Three distinct types of hotspots in the
553 Earth's mantle. Earth and Planetary Science Letters, 205(3-4), 295-308.

554 Craig, T. J., Jackson, J. A., Priestley, K., & McKenzie, D. (2011). Earthquake distribution
555 patterns in Africa: their relationship to variations in lithospheric and geological structure,
556 and their rheological implications. Geophysical Journal International, 185(1), 403-434.

557 Crisp, J. A. (1984). Rates of magma emplacement and volcanic output. Journal of Volcanology
558 and Geothermal Research, 20(3-4), 177-211.

559 DAAC, L. (2004). Global 30 Arc-Second Elevation Data Set GTOPO30. Land Process
560 Distributed Active Archive Center.

561 Dannberg, J., Gassmöller, R., Grove, R., & Heister, T. (2019). A new formulation for coupled
562 magma/mantle dynamics. Geophysical Journal International, 219(1), 94-107.

563 Dannberg, J., & Heister, T. (2016). Compressible magma/mantle dynamics: 3-D, adaptive
564 simulations in ASPECT. Geophysical Journal International, 207(3), 1343-1366.

565 Ebinger, C., Deino, A., Drake, R., & Tesha, A. (1989). Chronology of volcanism and rift basin
566 propagation: Rungwe volcanic province, East Africa. Journal of Geophysical Research:
567 Solid Earth, 94(B11), 15785-15803.

568 Ebinger, C., Deino, A., Tesha, A., Becker, T., & Ring, U. (1993). Tectonic controls on rift basin
569 morphology: evolution of the Northern Malawi (Nyasa) Rift. Journal of Geophysical
570 Research: Solid Earth, 98(B10), 17821-17836.

571 Ebinger, C., Djomani, Y. P., Mbede, E., Foster, A., & Dawson, J. B. (1997). Rifting archaean
572 lithosphere: the eyasi-manyara-natron rifts, east africa. Journal of the Geological Society,
573 154(6), 947-960.

574 Ebinger, C. J., Oliva, S. J., Pham, T. Q., Peterson, K., Chindandali, P., Illsley-Kemp, F., ... &
575 Gaherty, J. (2019). Kinematics of active deformation in the Malawi Rift and Rungwe
576 Volcanic Province, Africa. Geochemistry, Geophysics, Geosystems, 20(8), 3928-3951.

577 Ebinger, C., Rosendahl, B., & Reynolds, D. (1987). Tectonic model of the Malaŵi rift, Africa.
578 Tectonophysics, 141(1-3), 215-235.

579 Farr, T. G., Rosen, P. A., Caro, E., Crippen, R., Duren, R., Hensley, S., ... & Seal, D. (2007). The
580 shuttle radar topography mission. Reviews of geophysics, 45(2).

581 Fishwick, S. (2010). Surface wave tomography: imaging of the lithosphere–asthenosphere
582 boundary beneath central and southern Africa? Lithos, 120(1), 63-73.

583 Fontijn, K., Ernst, G. G., Elburg, M. A., Williamson, D., Abdallah, E., Kwelwa, S., ... & Jacobs,
584 P. (2010). Holocene explosive eruptions in the Rungwe volcanic province, Tanzania.
585 Journal of volcanology and geothermal research, 196(1-2), 91-110.

586 Fontijn, K., Williamson, D., Mbede, E., & Ernst, G. G. (2012). The Rungwe Volcanic Province,
587 Tanzania–A volcanological review. Journal of African Earth Sciences, 63, 12-31.

588 Furman, T. (2007). Geochemistry of East African Rift basalts: an overview. Journal of African
589 Earth Sciences, 48(2-3), 147-160.

590 Furman, T., Kaleta, K. M., Bryce, J. G., & Hanan, B. B. (2006). Tertiary mafic lavas of Turkana,
591 Kenya: constraints on East African plume structure and the occurrence of high-μ
592 volcanism in Africa. Journal of Petrology, 47(6), 1221-1244.

593 Gallagher, J., Potter, N., Sgouros, T., Hankin, S., & Flierl, G. (2004). The data access protocol—
594 DAP 2.0. http://www. opendap. org/.

595 Grijalva, A., Nyblade, A. A., Homman, K., Accardo, N. J., Gaherty, J. B., Ebinger, C. J., ... &
596 Mulibo, G. (2018). Seismic Evidence for Plume- and Craton- Influenced Upper Mantle
597 Structure Beneath the Northern Malawi Rift and the Rungwe Volcanic Province, East
598 Africa. Geochemistry, Geophysics, Geosystems, 19(10), 3980-3994.

599 Harkin, D. A. (1960). The Rungwe volcanics at the northern end of Lake Nyasa.

600 Heister, T., Dannberg, J., Gassmöller, R., & Bangerth, W. (2017). High accuracy mantle
601 convection simulation through modern numerical methods–II: realistic models and
602 problems. Geophysical Journal International, 210(2), 833-851.

603 Hilbert-Wolf, H., Roberts, E., Downie, B., Mtelela, C., Stevens, N. J., & O'Connor, P. (2017).
604 Application of U–Pb detrital zircon geochronology to drill cuttings for age control in
605 hydrocarbon exploration wells: A case study from the Rukwa Rift Basin, Tanzania.
606 AAPG Bulletin, 101(2), 143-159.

607 Hilton, D. R., Halldórsson, S. A., Barry, P. H., Fischer, T. P., de Moor, J. M., Ramirez, C. J., ...
608 & Scarsi, P. (2011). Helium isotopes at Rungwe Volcanic Province, Tanzania, and the
609 origin of East African plateaux. Geophysical Research Letters, 38(21).

610 Hirth, G., & Kohlstedt, D. (2004). Rheology of the upper mantle and the mantle wedge: A view
611 from the experimentalists. Inside the subduction Factory, 138, 83-105.

612 Jadamec, M. A., & Billen, M. I. (2010). Reconciling surface plate motions with rapid three-
613 dimensional mantle flow around a slab edge. Nature, 465(7296), 338-341.

614 Katz, R. F., Spiegelman, M., & Langmuir, C. H. (2003). A new parameterization of hydrous
615 mantle melting. Geochemistry, Geophysics, Geosystems, 4(9).

616 Keller, T., May, D. A., & Kaus, B. J. (2013). Numerical modelling of magma dynamics coupled
617 to tectonic deformation of lithosphere and crust. Geophysical Journal International,
618 195(3), 1406-1442.

619 Kendall, J. M., & Lithgow-Bertelloni, C. (2016). Why is Africa rifting?. Geological Society,
620 London, Special Publications, 420(1), 11-30.

621 Kendall, J. M., Stuart, G. W., Ebinger, C. J., Bastow, I. D., & Keir, D. (2005). Magma-assisted
622 rifting in Ethiopia. Nature, 433(7022), 146.

623 Koptev, A., Cloetingh, S., Gerya, T., Calais, E., & Leroy, S. (2018). Non-uniform splitting of a
624 single mantle plume by double cratonic roots: Insight into the origin of the central and
625 southern East African Rift System. Terra Nova, 30(2), 125-134.

626 Mckenzie, D. A. N., & Bickle, M. J. (1988). The volume and composition of melt generated by
627 extension of the lithosphere. Journal of petrology, 29(3), 625-679.

McKenzie, D. A. N., & O'NIONS, R. K. (1995). The source regions of ocean island basalts. Journal of petrology, 36(1), 133-159.

Mei, S., Bai, W., Hiraga, T., & Kohlstedt, D. L. (2002). Influence of melt on the creep behavior of olivine–basalt aggregates under hydrous conditions. Earth and Planetary Science Letters, 201(3-4), 491-507.

Mesko, G., Class, C., Maqway, M., Boniface, N., Manya, S., & Hemming, S. (2014). The Timing of Early Magmatism and Extension in the Southern East African Rift: Tracking Geochemical Source Variability with 40Ar/39Ar Geochronology at the Rungwe Volcanic Province, SW Tanzania. Paper presented at the AGU Fall Meeting Abstracts, V51A-4730.

Mesko, G. (2020). Magmatism at the Southern End of the East African Rift System: Origin and Role During Early Stage Rifting (Doctoral dissertation, Columbia University).

Nielsen, T. K., & Hopper, J. R. (2002). Formation of volcanic rifted margins: Are temperature anomalies required?. Geophysical Research Letters, 29(21), 18-1.

Njinju, E. A., Kolawole, F., Atekwana, E. A., Stamps, D. S., Atekwana, E. A., Abdelsalam, M. G., & Mickus, K. L. (2019). Terrestrial heat flow in the Malawi Rifted Zone, East Africa: Implications for tectono-thermal inheritance in continental rift basins. Journal of Volcanology and Geothermal Research, 387, 106656.

Njinju, E. A., Atekwana, E. A., Stamps, D. S., Abdelsalam, M. G., Atekwana, E. A., Mickus, K. L., ... & Nyalugwe, V. N. (2019). Lithospheric Structure of the Malawi Rift: Implications for Magma- Poor Rifting Processes. Tectonics, 38(11), 3835-3853.

649 Rajaonarison, T. A., Stamps, D. S., Fishwick, S., Brune, S., Glerum, A., & Hu, J. (2020).
650 Numerical Modeling of Mantle Flow Beneath Madagascar to Constrain Upper Mantle
651 Rheology Beneath Continental Regions. Journal of Geophysical Research. Solid Earth,
652 125(2), Art-No.

653 Roberts, E. M., Stevens, N. J., O'Connor, P. M., Dirks, P. H. G. M., Gottfried, M. D., Clyde, W.
654 C., ... & Hemming, S. (2012). Initiation of the western branch of the East African Rift
655 coeval with the eastern branch. Nature Geoscience, 5(4), 289-294.

656 Rooney, T. O., Herzberg, C., & Bastow, I. D. (2012). Elevated mantle temperature beneath East
657 Africa. Geology, 40(1), 27-30.

658 Rose, I., Buffett, B., & Heister, T. (2017). Stability and accuracy of free surface time integration
659 in viscous flows. Physics of the Earth and Planetary Interiors, 262, 90-100.

660 Saria, E., Calais, E., Stamps, D., Delvaux, D., & Hartnady, C. (2014). Present- day kinematics of
661 the East African Rift. Journal of Geophysical Research: Solid Earth, 119(4), 3584-3600.

662 Saunders, A. D., Storey, M., Kent, R. W., & Norry, M. J. (1992). Consequences of plume-
663 lithosphere interactions. Geological Society, London, Special Publications, 68(1), 41-60.

664 Stamps, D. S., Calais, E., Saria, E., Hartnady, C., Nocquet, J. M., Ebinger, C. J., & Fernandes, R.
665 M. (2008). A kinematic model for the East African Rift. Geophysical Research Letters,
666 35(5).

667 Van Wijk, J. W., Huismans, R. S., Ter Voorde, M., & Cloetingh, S. A. P. L. (2001). Melt
668 generation at volcanic continental margins: no need for a mantle plume?. Geophysical
669 Research Letters, 28(20), 3995-3998.

Wessel, P., Smith, W. H., Scharroo, R., Luis, J., & Wobbe, F. (2013). Generic mapping tools: improved version released. Eos, Transactions American Geophysical Union, 94(45), 409-410.

White, R., & McKenzie, D. (1989). Magmatism at rift zones: the generation of volcanic continental margins and flood basalts. Journal of Geophysical Research: Solid Earth, 94(B6), 7685-7729.

Yang, H., Chemia, Z., Artemieva, I. M., & Thybo, H. (2018). Control on off-rift magmatism: A case study of the Baikal Rift Zone. Earth and Planetary Science Letters, 482, 501-509.

Yu, Y., Gao, S. S., Zhao, D., & Liu, K. H. (2020). Mantle Structure and Flow Beneath an Early- Stage Continental Rift: Constraints From P Wave Anisotropic Tomography. Tectonics, 39(2), e2019TC005590.